

Multimodal Deep Unfolding for Guided Image Super-Resolution

Iman Marivani, *Student Member, IEEE*, Evaggelia Tsiligiani, *Member, IEEE*, Bruno Cornelis, *Member, IEEE*, and Nikos Deligiannis, *Member, IEEE*

Abstract—The reconstruction of a high resolution image given a low resolution observation is an ill-posed inverse problem in imaging. Deep learning methods rely on training data to learn an end-to-end mapping from a low-resolution input to a high-resolution output. Unlike existing deep multimodal models that do not incorporate domain knowledge about the problem, we propose a multimodal deep learning design that incorporates sparse priors and allows the effective integration of information from another image modality into the network architecture. Our solution relies on a novel deep unfolding operator, performing steps similar to an iterative algorithm for convolutional sparse coding with side information; therefore, the proposed neural network is interpretable by design. The deep unfolding architecture is used as a core component of a multimodal framework for guided image super-resolution. An alternative multimodal design is investigated by employing residual learning to improve the training efficiency. The presented multimodal approach is applied to super-resolution of near-infrared and multi-spectral images as well as depth upsampling using RGB images as side information. Experimental results show that our model outperforms state-of-the-art methods.

Index Terms—multimodal deep unfolding, multimodal image super-resolution, interpretable convolutional neural networks.

I. INTRODUCTION

IMAGE super-resolution (SR) is a well-known inverse problem in imaging, referring to the reconstruction of a high-resolution (HR) image from a low-resolution (LR) observation [1], [2]. The problem is ill-posed as there is no unique mapping from the LR to the HR image. Practical applications such as medical imaging and remote sensing often involve different image modalities capturing the same scene, therefore, another approach in imaging is the joint use of multiple image modalities. The problem of multimodal or guided image super-resolution refers to the reconstruction of an HR image from an LR observation using a *guidance* image from another modality, also referred to as *side information*.

Several image processing methods use prior knowledge about the image such as sparse structure [3]–[9] or statistical image priors [10], [11]. Deep learning has been widely used in inverse problems, often outperforming analytical methods [2], [12]. For instance, in single image SR, Convolutional Neural Networks (CNNs) have led to impressive results reported in [13]–[18]. Residual learning [19] enabled the training of very deep neural networks (DNNs), with the models proposed in [20]–[24] achieving state-of-the-art performance.

Capturing the correlation among different image modalities has been addressed with sparsity-based analytical models and coupled dictionary learning [25]–[33]. The main drawback of these approaches is the high-computational cost of iterative algorithms for sparse approximation, which has been addressed by multimodal deep learning methods [34]–[36]. A common approach in multimodal neural network design is the fusion of the input modalities at a shared latent layer, obtained as the concatenation of the latent representations of each modality [34]. The CNN model proposed in [35] for multimodal depth upsampling follows this principle. Nevertheless, current multimodal DNNs are black-box models in the sense that we lack a principled approach to design such models for leveraging the signal structure and properties of the correlation across modalities.

A recent line of research in deep learning for inverse problems considers *deep unfolding* [37]–[42], that is, the unfolding of an iterative algorithm into the form of a DNN. Inspired by numerical algorithms for sparse coding, deep unfolding designs have been utilized in several imaging problems to incorporate sparse priors into the solution. Results for denoising [42], compressive imaging [43], and image SR [44] have shown that incorporating domain knowledge into the network architecture can improve the performance substantially. Still, these methods focus on single-modal data, thereby lacking a principled way to incorporate knowledge from different imaging modalities. To the best of our knowledge, the only deep unfolding designs for guided image SR have been presented in [45] and [46], that build upon existing unfolding architectures for learned sparse coding [37] and learned convolutional sparse coding [42], respectively.

In this paper, we address the problem of guided image SR with a novel multimodal deep unfolding architecture, which is inspired by a proximal algorithm for convolutional sparse coding with side information. The proximal algorithm is translated into a neural network form coined Learned Multimodal Convolutional Sparse Coding (LMCSC); the network incorporates sparse priors and enables efficient integration of the guidance modality into the solution. While in existing multimodal deep learning methods [34]–[36], it is difficult to understand what the model has learned, our deep neural network is interpretable, in the sense that the model performs steps similar to an iterative algorithm.

The proposed approach builds upon our previous research on multimodal deep unfolding [47], [48], and preliminary results of LMCSC can be found in [49], where the recovery of HR near infrared (NIR) images based on LR NIR observations

The authors are with the Department of Electronics and Informatics, Vrije Universiteit Brussel, 1050 Brussels and with imec, Kapeldreef 75, 3001 Leuven, Belgium. (e-mail: {imarivan, etsiligi, bcorneli, ndeligia}@etrovub.be)

with the aid of RGB images was addressed. In this paper, we integrate LMCS into different neural network architectures, and present experiments on various multimodal datasets, showing the superior performance of the proposed approach against several single- and multimodal SR methods. Our contribution is as follows:

- (i) We formulate the problem of convolutional sparse coding with side information, and propose a proximal algorithm for its solution.
- (ii) Inspired by the proposed proximal algorithm, we design a deep unfolding neural network for fast computation of convolutional sparse codes with the aid of side information.
- (iii) The deep unfolding operator is used as a core component in a novel multimodal framework for guided image SR that fuses information from two image modalities. Furthermore, we exploit residual learning and introduce skip connections in the proposed framework, obtaining an alternative design that can be trained more efficiently.
- (iv) We test our models on several benchmark multimodal datasets, including NIR/RGB, multi-spectral/RGB, depth/RGB, and compare them against various state-of-the-art single-modal and multimodal models. The numerical results show a PSNR gain of up to 2.74dB over the coupled ISTA method in [45].

The rest of the paper is organized as follows: Section II reviews related work and Section III provides the necessary background. Section IV presents the proposed core deep unfolding architecture for convolutional sparse coding with side information, and our designs for multimodal image SR are presented in Section V, followed by experimental results in Section VI. Section VII concludes the paper.

Throughout the paper, all vectors are denoted by boldface lower case letters while lower case letters are used for scalars. We utilize boldface upper case letters to show matrices and boldface upper case letters in math calligraphy to indicate tensors. Moreover, in this paper, the terms upscaling factor and scale are used interchangeably.

II. RELATED WORK

1) *Single Image Super-Resolution*: A first category of single image SR methods includes interpolation-based methods [11], [50]–[52]. These methods are simple and fast, however, aliasing and blurring effects make them inefficient in obtaining HR images of fine quality. A second category includes reconstruction methods [53]–[55], which use several image priors to regularize the ill-posed reconstruction problem and result in images with fine texture details. Nevertheless, modelling the complex context of natural images with image priors is not an easy task. A third popular category consists of learning-based methods [3]–[8], [13]–[18], [20]–[24], which use machine learning techniques to learn the complex mapping between LR and HR images from data.

Among learning based methods, deep learning models have drawn considerable attention as they achieve excellent restoration quality. SRCNN [13] was the first deep learning

method for image SR. The model has a simple structure and can directly learn an end-to-end mapping between the LR/HR images. An accelerated version of [13] was presented in [14]. Increasing the depth of CNN architectures ensues several training difficulties which have been mitigated with residual learning. Examples of very deep residual networks for SR include a 20-layer CNN proposed in [15], [16], a 30-layer convolutional autoencoder proposed in [17], and a 52-layer CNN proposed in [22]. Residual learning has also been employed to learn inter-layer dependencies in [23], [24]. An improved residual design obtained by removing unnecessary residual modules was proposed in [20]. Recurrent neural networks (RNNs) have been also used for image SR in [56], [57]. The network in [56] implements a feedback mechanism that carries high-level information back to previous layers, refining low-level encoded information. Following [56], the authors of [57] presented an alternative structure with two states (RNN layers) that operate at different spatial resolutions, providing information flow from LR to HR encodings.

Deep unfolding has been applied to single image SR in [44] where the authors designed a neural network that computes latent representations of the LR/HR image using LISTA [37], a neural network that performs steps similar to the Iterative Soft Thresholding Algorithm (ISTA) [58] (see also Section III).

2) *Multimodal Image Super-Resolution*: A common approach in multimodal image restoration is the joint or guided filtering approach, that is, the design of a filter that leverages the guidance image as a prior and transfers structural details from the guidance to the target image. Several joint filtering techniques have been proposed in [59]–[61]. Nevertheless, when the local structures in the guidance and target images are not consistent, these techniques may transfer incorrect content to the target image. The approach presented in [62] concerns the design of an explicit mapping that captures the structural discrepancy between images from different modalities.

Model-based techniques and joint filtering methods are limited in characterizing the complex dependency between different modalities. Learning based methods aim to learn this dependency from data. In a depth upsampling method presented in [63], a weighted analysis representation is used to model the complex relationship between depth and RGB images; the model parameters are learned with a task driven training strategy. Another learning based approach relies on sparse modelling and involves coupled-dictionary learning [25]–[32]. Most of these works assume that there is a mapping between the sparse representation of one modality to the sparse representation of another modality. The authors of [33] consider both similarities and disparities between different modalities under the sparse representation invariance assumption.

Purely data-driven solutions for multimodal image SR are provided by multimodal deep learning approaches. Examples include the model presented in [35] implementing a CNN based joint image filter, and the work presented in [36], which is a deep learning reformulation of the widely used guided image filter proposed in [60].

The deep unfolding design LISTA [37] has also been deployed for multimodal image SR in [45] where a coupled ISTA network is presented. The network accepts as input an

LR image from the target modality and an HR image from the guidance modality. Two LISTA branches are employed to compute latent representations of the input images. The estimation of the target HR image is obtained as a linear combination of these representations. A similar approach is proposed in [46] that employs three convolutional LISTA networks to split the common information shared between modalities, from the unique information belonging to each modality. The output is then computed as a combination of these common and unique feature maps after applying the corresponding dictionaries on them.

III. BACKGROUND

Image super-resolution can be addressed as a linear inverse problem formulated as follows [3]:

$$\mathbf{y} = \mathbf{L}\mathbf{x} + \boldsymbol{\eta}, \quad (1)$$

where $\mathbf{x} \in \mathbb{R}^k$ is a vectorized form of the unknown HR image, and $\mathbf{y} \in \mathbb{R}^n$ denotes the LR observations contaminated with noise $\boldsymbol{\eta} \in \mathbb{R}^n$. The linear operator $\mathbf{L} \in \mathbb{R}^{n \times k}$, $n < k$, describes the observation mechanism, which can be expressed as the product of a downsampling operator \mathbf{E} and a blurring filter \mathbf{H} [3]. Problem (1) appears in many imaging applications including image restoration and inpainting [1], [2].

A. Image Super-Resolution via Sparse Approximation

Even when the linear observation operator \mathbf{L} is given, problem (1) is ill-posed and requires additional regularization for its solution. Sparsity has been widely used as a regularizer leading to the well-known sparse approximation problem [64]. Instead of directly solving for \mathbf{x} , in this paper, we rely on a sparse modelling approach presented in [3]. According to [3], an n -dimensional (vectorized) patch \mathbf{y} from a bicubic-upscaled LR image and the corresponding patch \mathbf{x} from the respective HR image can be expressed by joint sparse representations. By jointly learning two dictionaries $\Psi_{\mathbf{y}} \in \mathbb{R}^{n \times m}$, $\Psi_{\mathbf{x}} \in \mathbb{R}^{n \times m}$, $n \leq m$, for the low- and the high-resolution image patches, respectively, we can enforce the similarity of sparse representations of patch pairs such that $\mathbf{y} = \Psi_{\mathbf{y}}\boldsymbol{\alpha}$ and $\mathbf{x} = \Psi_{\mathbf{x}}\boldsymbol{\alpha}$, $\boldsymbol{\alpha} \in \mathbb{R}^m$. Then, computing the HR patch \mathbf{x} is equivalent to finding the sparse representation of the LR patch \mathbf{y} , by solving

$$\min_{\boldsymbol{\alpha}} \frac{1}{2} \|\mathbf{y} - \Psi_{\mathbf{y}}\boldsymbol{\alpha}\|_2^2 + \lambda \|\boldsymbol{\alpha}\|_1, \quad (2)$$

where λ is a regularization parameter, and $\|\boldsymbol{\alpha}\|_1 = \sum_{i=1}^k |\alpha_i|$ is the ℓ_1 -norm, which promotes sparsity. Several methods have been proposed for solving (2) including pivoting algorithms, interior-point methods and gradient based methods [64].

Sparse modelling techniques that involve computations applied to independent image patches do not take into account the consistency of pixels in overlapping patches [9]. Convolutional Sparse Coding (CSC) [65] is an alternative approach, which can be directly applied to the entire image. Denoting with $\mathbf{Y} \in \mathbb{R}^{n_1 \times n_2}$ the image of interest, the convolutional sparse codes are obtained by solving the following problem:

$$\min_{\mathbf{U}_i} \frac{1}{2} \|\mathbf{Y} - \sum_{i=1}^k \mathbf{D}_i * \mathbf{U}_i\|_F^2 + \lambda \sum_{i=1}^k \|\mathbf{U}_i\|_1, \quad (3)$$

where $\|\mathbf{A}\|_F = \sqrt{\sum_i \sum_j |a_{ij}|^2}$ is the Frobenius norm, $\mathbf{D}_i \in \mathbb{R}^{p_1 \times p_2}$, $i = 1, \dots, k$, are the atoms of a convolutional dictionary $\mathcal{D} \in \mathbb{R}^{p_1 \times p_2 \times k}$, and $\mathbf{U}_i \in \mathbb{R}^{n_1 \times n_2}$, $i = 1, \dots, k$, are the sparse feature maps with respect to \mathcal{D} . The ℓ_1 -norm computes the sum of absolute values of the elements in \mathbf{U}_i (as if \mathbf{U}_i is unrolled as a vector). Efficient solutions of (3) are presented in [66], [67].

According to recent studies [68], the accuracy of sparse approximation problems can be improved if a signal $\boldsymbol{\omega}$ correlated with the target signal \mathbf{y} is available; we refer to $\boldsymbol{\omega}$ as side information (SI). Assume that $\mathbf{y} \in \mathbb{R}^n$ and $\boldsymbol{\omega} \in \mathbb{R}^d$ have similar sparse representations $\boldsymbol{\alpha} \in \mathbb{R}^m$, $\mathbf{s} \in \mathbb{R}^m$, under dictionaries $\Psi_{\mathbf{y}} \in \mathbb{R}^{n \times m}$, $\Psi_{\boldsymbol{\omega}} \in \mathbb{R}^{d \times m}$, $n \leq m$, $d \leq m$, respectively. Then the sparse representation $\boldsymbol{\alpha}$ can be obtained as the solution of the ℓ_1 - ℓ_1 minimization problem [68].

$$\min_{\boldsymbol{\alpha}} \frac{1}{2} \|\mathbf{y} - \Psi_{\mathbf{y}}\boldsymbol{\alpha}\|_2^2 + \lambda (\|\boldsymbol{\alpha}\|_1 + \|\boldsymbol{\alpha} - \mathbf{s}\|_1). \quad (4)$$

Problem (4) has been theoretically studied in [68]. Numerical methods for its solution are presented in [69], [70].

B. Deep Unfolding

Analytical approaches for sparse approximation are usually equipped with theoretical guarantees; however, their major drawback is their high computational complexity. In some applications, the deployed dictionaries also need to be learned, increasing the computational burden [3]. The authors of [37] address this problem by a neural network design that performs operations similar to the Iterative Soft Thresholding Algorithm (ISTA) [58] proposed for the solution of (2). The learning process results in a trained version of ISTA, coined LISTA. The t -th layer of LISTA computes:

$$\boldsymbol{\alpha}^t = \phi_{\gamma}(\mathbf{S}\boldsymbol{\alpha}^{t-1} + \mathbf{W}\mathbf{y}), \quad \boldsymbol{\alpha}^0 = 0, \quad (5)$$

where

$$\phi_{\gamma}(v_i) = \text{sign}(v_i) \max\{0, |v_i| - \gamma\}, \quad i = 1, \dots, k, \quad (6)$$

is the soft thresholding operator; $\mathbf{S} \in \mathbb{R}^{m \times m}$, $\mathbf{W} \in \mathbb{R}^{m \times n}$ and $\gamma > 0$ are parameters, which are fixed in ISTA, while LISTA learns them from data. As a result, LISTA achieves high accuracy in only a few iterations. The technique known as deep unfolding was also explored in [38]–[41]; a convolutional LISTA design for CSC was presented in [42].

The aforementioned deep unfolding studies deal with single-modal data. A deep unfolding design that incorporates side information coming from another modality was first presented in our previous work [47]. The model proposed in [47] relies on a proximal method for the solution of (4), which iterates over

$$\boldsymbol{\alpha}^t = \xi_{\mu} \left(\left(\mathbf{I} - \frac{1}{L} \Psi^T \Psi \right) \boldsymbol{\alpha}^{t-1} + \frac{1}{L} \Psi^T \mathbf{y}; \mathbf{s} \right), \quad \boldsymbol{\alpha}^0 = 0, \quad (7)$$

with μ , L appropriate parameters. The proximal operator ξ_{μ} incorporates the side information \mathbf{s} and is expressed as follows:

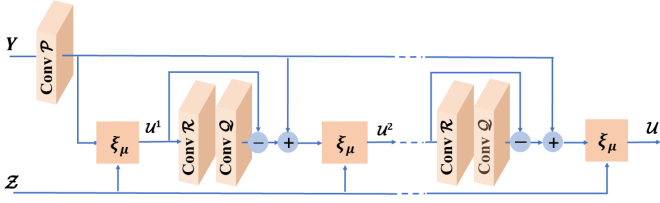


Fig. 1. The proposed LMCSC model with unfolded recurrent stages. The model computes sparse feature maps \mathbf{U} of an image \mathbf{Y} given sparse feature maps \mathbf{Z} of the side information. The nonlinear activation function follows the proximal operator $\xi_\mu(v; z)$ given by (8), (9).

- 1) For $s_i \geq 0, i = 1, \dots, m$:

$$\xi_\mu(v_i; s_i) = \begin{cases} v_i + 2\mu, & v_i < -2\mu \\ 0, & -2\mu \leq v_i \leq 0 \\ v_i, & 0 < v_i < s_i \\ s_i, & s_i \leq v_i \leq s_i + 2\mu \\ v_i - 2\mu, & v_i \geq s_i + 2\mu \end{cases} \quad (8)$$

- 2) For $s_i < 0, i = 1, \dots, m$:

$$\xi_\mu(v_i; s_i) = \begin{cases} v_i + 2\mu, & v_i < s_i - 2\mu \\ s_i, & s_i - 2\mu \leq v_i \leq s_i \\ v_i, & s_i < v_i < 0 \\ 0, & 0 \leq v_i \leq 2\mu \\ v_i - 2\mu, & v_i \geq 2\mu \end{cases} \quad (9)$$

By writing the proximal algorithm in the form

$$\alpha^t = \xi_\mu(\mathbf{S}\alpha^{t-1} + \mathbf{W}\mathbf{y}; \mathbf{s}), \quad \alpha^0 = 0, \quad (10)$$

and translating (10) into a deep neural network, we obtain a fast multimodal operator referred to as Learned Side-Information-driven iterative soft Thresholding Algorithm (LeSITA). LeSITA has a similar expression to LISTA (5), however, (10) employs the new activation function ξ_μ that integrates side information into the learning process.

IV. DESIGN MULTIMODAL CONVOLUTIONAL NETWORKS WITH DEEP UNFOLDING

In what follows, we consider that, besides the observations \mathbf{Y} of the target signal, another image modality Ω , correlated with \mathbf{Y} is available. We assume that the two image modalities can be represented by convolutional sparse codes that are similar by means of the ℓ_1 -norm. Specifically, let $\mathbf{Y} = \sum_{i=1}^k \mathbf{D}_i^Y * \mathbf{U}_i$ be a sparse representation of the observed image \mathbf{Y} with respect to a convolutional dictionary \mathcal{D}^Y ; $\mathbf{D}_i^Y \in \mathbb{R}^{n_1 \times n_2}$, $i = 1, \dots, k$, denote the atoms of \mathcal{D}^Y . By employing a convolutional dictionary \mathcal{D}^Ω with atoms $\mathbf{D}_i^\Omega \in \mathbb{R}^{p_1 \times p_2}$, $i = 1, \dots, k$, the guidance image $\Omega \in \mathbb{R}^{n_1 \times n_2}$ can be expressed as $\Omega = \sum_{i=1}^k \mathbf{D}_i^\Omega * \mathbf{Z}_i$ with the convolutional sparse codes \mathbf{Z}_i , $i = 1, \dots, k$, obtained as the solution of (3). Then, we can compute the unknown sparse codes \mathbf{U}_i of the target modality by solving a problem formulated in a way similar to (4), that is,

$$\min_{\mathbf{U}_i} \frac{1}{2} \left\| \mathbf{Y} - \sum_{i=1}^k \mathbf{D}_i^Y * \mathbf{U}_i \right\|_F^2 + \lambda \left(\sum_{i=1}^k \|\mathbf{U}_i\|_1 + \sum_{i=1}^k \|\mathbf{U}_i - \mathbf{Z}_i\|_1 \right). \quad (11)$$

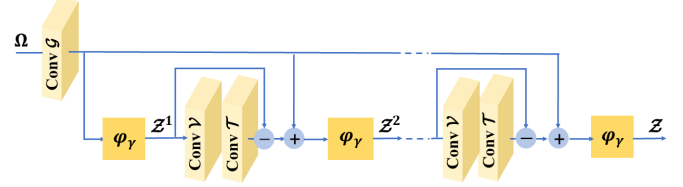


Fig. 2. The Approximate Convolutional Sparse Coding (ACSC) model [42] is used to encode the side information. The nonlinear activation function follows the proximal operator $\phi_\gamma(v)$ in (6).

There is a correspondence between convolutional and linear sparse codes. If we replace the convolutional dictionary \mathcal{D}^Y with a matrix \mathbf{A} with Toeplitz structure, and take into account the linear properties of convolution, then (11) reduces to (4). Specifically, we define $\mathbf{A} \in \mathbb{R}^{(n_1-p_1+1)(n_2-p_2+1) \times kn_1n_2}$ as a sparse dictionary obtained by concatenating the Toeplitz matrices that unroll \mathbf{D}_i^Y 's; $\alpha \in \mathbb{R}^{kn_1n_2}$ and $\mathbf{s} \in \mathbb{R}^{kn_1n_2}$ take the form of vectorized sparse feature maps of the target and the side information images, respectively. Then, by replacing the convolutional operations in (11) with multiplications, we obtain (4), and the proximal algorithm (7) can be employed to compute convolutional sparse codes.

Nevertheless, transforming (11) to (4) and using (7) for its solution is not computationally efficient. Since CSC deals with the entire image, the dimensionality of (4) becomes too high and the proximal method becomes impractical. We use the correspondence between linear and convolutional representations, and formulate an iterative algorithm that performs convolutions as follows: In the proximal algorithm (7), the matrices \mathbf{A} and \mathbf{A}^T , which take the form of concatenated Toeplitz matrices in the convolutional case, are replaced by the convolutional dictionaries \mathcal{B}^Y and $\tilde{\mathcal{B}}^Y$, respectively. Then, by replacing multiplications with convolutional operations, we can compute the convolutional codes \mathbf{U} of the target image, given the convolutional codes \mathbf{Z} of the guidance image, by iterating over:

$$\mathbf{U}^t = \xi_\mu(\mathbf{U}^{t-1} - \tilde{\mathcal{B}}^Y * \mathcal{B}^Y * \mathbf{U}^{t-1} + \tilde{\mathcal{B}}^Y * \mathbf{Y}; \mathbf{Z}), \quad (12)$$

where \mathbf{U} , \mathbf{Z} are tensors of size $p_1 \times p_2 \times k$.

Equation (12) can be translated into a deep convolutional neural network (CNN). Each stage of the network computes the sparse feature maps according to

$$\mathbf{U}^t = \xi_\mu(\mathbf{U}^{t-1} - \mathcal{Q} * \mathcal{R} * \mathbf{U}^{t-1} + \mathcal{P} * \mathbf{Y}; \mathbf{Z}), \quad (13)$$

with $\mathcal{Q} \in \mathbb{R}^{p_1 \times p_2 \times c \times k}$, $\mathcal{R} \in \mathbb{R}^{p_1 \times p_2 \times k \times c}$, $\mathcal{P} \in \mathbb{R}^{p_1 \times p_2 \times c \times k}$ learnable convolutional layers and $\mu > 0$ a learnable parameter; c is the number of channels of the employed images. The proposed network architecture, depicted in Fig. 1, is referred to as Learned Multimodal Convolutional Sparse Coding (LM-CSC). The network can be trained in a supervised manner to map an input image to sparse feature maps. During training, the parameters \mathcal{Q} , \mathcal{R} , \mathcal{P} and μ are learned; therefore, the deep LMCSC can achieve high accuracy with only a fraction of computations of the proximal method.

LMCSC uses the convolutional sparse codes \mathbf{Z} of the guidance modality Ω to compute the convolutional sparse

codes of the target modality \mathbf{Y} . An efficient multimodal convolutional operator should integrate a fast operator for the encoding of the guidance modality. In the models presented next, we obtain \mathbf{Z} using the ACSC operator presented in [42]. ACSC has the form of convolutional LISTA, with the t -th layer computing:

$$\mathbf{Z}^t = \phi_\gamma(\mathbf{Z}^{t-1} - \mathcal{T} * \mathcal{V} * \mathbf{Z}^{t-1} + \mathcal{G} * \Omega), \quad (14)$$

where ϕ_γ is the proximal operator given by (6). The parameters of the convolutional layers $\mathcal{T} \in \mathbb{R}^{p_1 \times p_2 \times c \times k}$, $\mathcal{G} \in \mathbb{R}^{p_1 \times p_2 \times c \times k}$ and $\mathcal{V} \in \mathbb{R}^{p_1 \times p_2 \times k \times c}$, are learned from data. The architecture of ACSC is depicted in Fig. 2.

V. DEEP MULTIMODAL IMAGE SUPER-RESOLUTION

The proposed LMCSC architecture can be employed to perform multimodal image super-resolution based on a sparsity-driven convolutional model. The proposed model follows similar principles with [3]. Specifically, the sparse linear modelling of LR/HR image patches presented in [3] is replaced by a sparse convolutional modelling of the entire LR/HR images, followed by similarity assumptions between the convolutional representations of the LR and HR images. To efficiently integrate information from a second image modality, we also assume that the target and the guidance image modalities are similar by means of the ℓ_1 -norm in the representation domain.

A. LMCSC-Net

Our first model proposed for multimodal image super-resolution relies on the following assumption: The LR observation \mathbf{Y} and the HR image \mathbf{X} share the same convolutional sparse features maps \mathbf{U}_i , under different convolutional dictionaries \mathcal{D}^Y and \mathcal{D}^X , that is, $\mathbf{Y} = \sum_{i=1}^k \mathcal{D}_i^Y * \mathbf{U}_i$, $\mathbf{X} = \sum_{i=1}^k \mathcal{D}_i^X * \mathbf{U}_i$, where \mathcal{D}_i^Y , \mathcal{D}_i^X are the atoms of the respective convolutional dictionaries. Given \mathcal{D}^Y , \mathcal{D}^X , finding a mapping from \mathbf{Y} to \mathbf{X} is equivalent to computing the sparse features maps \mathbf{U} of the observed LR image \mathbf{Y} . The similarity assumption between the target and the guidance image modalities in the representation domain implies that the convolutional sparse codes \mathbf{Z} of the guidance HR image Ω are similar to \mathbf{U} by means of the ℓ_1 -norm. Therefore, \mathbf{U} can be obtained as the solution of the ℓ_1 - ℓ_1 minimization problem (11). Based on these assumptions, we build our first model for multimodal image SR using LMCSC as a core component of a deep architecture.

The proposed model, coined LMCSC-Net, consists of three subnetworks: (i) an LMCSC encoder that produces convolutional latent representations of the input LR image with the aid of side information, (ii) a side information encoder that produces latent representations of the guidance HR image, and (iii) a convolutional decoder that computes the target HR image. The goal of the LMCSC encoder is to learn a convolutional sparse feature map \mathbf{U} of the LR image \mathbf{Y} , also shared by the HR image \mathbf{X} , using a convolutional sparse feature map \mathbf{Z} as side information, akin to the model presented in Section IV. The LMCSC branch is followed by a convolutional decoder realized by a learnable convolutional dictionary \mathcal{D}^X .

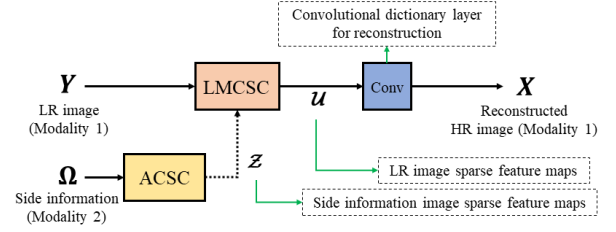


Fig. 3. The proposed LMCSC-Net, a deep multimodal SR network consisting of an LMCSC encoder, an ACSC side information encoder, and a convolutional decoder.

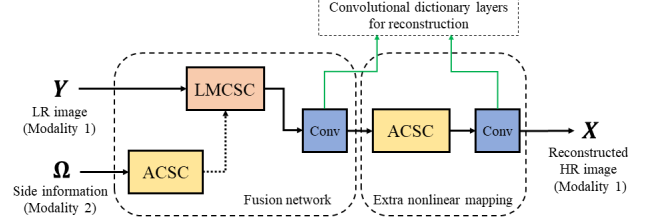


Fig. 4. The proposed LMCSC+-Net, a deep multimodal SR network consisting of an LMCSC component with an additional ACSC branch performing enhancement of the LR/HR mapping.

The decoder receives the latent representations \mathbf{U} provided by LMCSC and estimates \mathbf{X} according to $\hat{\mathbf{X}} = \mathcal{D}^X * \mathbf{U}$.

The entire network, depicted in Fig. 3, is trained end-to-end using the mean square error (MSE) loss function:

$$\min_{\Theta} \sum_i \|\hat{\mathbf{X}}_i - \mathbf{X}_i\|_F^2, \quad (15)$$

where Θ denotes the set of all network parameters, \mathbf{X}_i is the ground-truth image of the target modality, and $\hat{\mathbf{X}}_i$ is the estimation computed by the network.

Different from our previous multimodal image SR design [48] which relies on LeSITA [47], LMCSC-Net has a novel convolutional structure inspired by a different proximal algorithm. The core LMCSC component computes latent representations of the target modality using side information from the guidance modality, performing fusion of information at every layer. Therefore, our approach is different from coupled ISTA [45] which employs one branch of LISTA [37] for each modality and fuses the latent representations only in the last layer.

B. LMCSC+-Net

The model presented in Section V-A learns similar sparse representations of three different image modalities, that is, the input LR image \mathbf{Y} , the guidance modality Ω and the HR image \mathbf{X} . Learning representations that mainly encode the common information among the different modalities is critical for the performance of the model. Nevertheless, some information from the guidance modality may be misleading when learning a mapping between \mathbf{X} and \mathbf{Y} . In other words, the encoding performed by the ACSC branch may result in transferring unrelated information to the LMCSC encoder. As a result, the latent representation of the target modality may

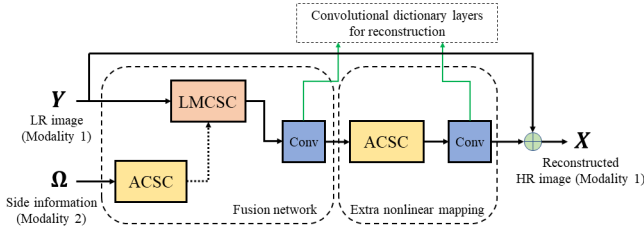


Fig. 5. The proposed LMCS-ResNet, a deep multimodal LMCS-Net-based network with a skip connection.

not capture the underlying mapping between the LR and HR images in the representation domain. Furthermore, assuming identical latent representations for both LR and HR images limits the performance of the network especially when the degradation level of the LR observations is high.

In order to address the aforementioned problems, we relax the assumption concerning the similarity between the LR and HR images in the representation domain. Specifically, we assume that the convolutional sparse codes \mathbf{U}_x of the HR image \mathbf{X} can be obtained as a non-linear transformation of the respective codes \mathbf{U}_y of the LR image \mathbf{Y} , that is, $\mathbf{U}_x = F_{\Theta'}(\mathbf{U}_y)$ where $F_{\Theta'}$ is a non-linear function parameterized by Θ' .

Under this assumption, we build the proposed multimodal SR framework by employing the following components: (i) An LMCS-Net subnetwork is used to fuse the information from the LR observations and the guidance HR image, providing a first estimation of the target HR image with the aid of side information. (ii) An ACSC subnetwork following the LMCS-Net subnetwork is used to enhance the transformation between the LR and HR images of the target modality without using side information. The architecture of the proposed model, referred to as LMCS-Net₊, is depicted in Fig. 4. The additional ACSC and dictionary layers in LMCS-Net₊ implement $F_{\Theta'}$. The network is trained using the objective (15).

C. LMCS-Net with Skip Connections

Considering the significant improvement achieved by residual learning in the training efficiency and the prediction accuracy [19]–[24], we enhance the proposed LMCS-Net₊ with a skip connection, introducing a new model coined LMCS-ResNet. For the design of LMCS-ResNet we rely on the assumption that the HR image \mathbf{X} contains all the low-frequency information from the LR image \mathbf{Y} plus some high-frequency details that can be captured by a non-linear mapping between LR and HR images. By using an identity mapping of the input, the capacity of the network can be assigned to learning the high frequency details, since the low-frequency information is provided by \mathbf{Y} . LMCS-ResNet learns the non-linear mapping $H(\mathbf{Y}, \Omega) = F(\mathbf{Y}, \Omega) + \mathbf{Y}$, where $F(\mathbf{Y}, \Omega) = \hat{\mathbf{X}} - \mathbf{Y}$. In LMCS-ResNet, $F(\mathbf{Y}, \Omega)$ is obtained from the LMCS-Net₊. The model architecture is presented in Fig. 5. This model is also trained end-to-end using the objective (15).

VI. EXPERIMENTS

We apply the proposed models to different upsampling tasks, that is, super-resolution of near-infrared (NIR) images, depth upsampling and super-resolution of multi-spectral data, using RGB images as side information. We compare our models against state-of-the-art single-modal and multimodal methods showing the superior performance of the proposed approach. Before demonstrating our experimental results, we present the employed datasets and report implementation details.

A. Datasets

1) *EPFL RGB-NIR dataset*: NIR images are acquired at a low resolution due to the high cost per pixel of a NIR sensor compared to an RGB sensor. We employ the EPFL RGB-NIR dataset¹ and apply our models to super-resolve an LR NIR image with the aid of an HR RGB image. The dataset contains 477 spatially aligned NIR/RGB image pairs. Our training set contains approximately 30,000 cropped image pairs extracted from 50 images. Each training image is of size 44×44 pixels; the size is chosen with respect to memory requirements and computational complexity. We also create a testing set containing 25 image pairs; testing is performed on an entire image.

The NIR images consist of one channel. An LR version of a NIR image is generated by blurring and downscaling the ground truth HR version. We convert the RGB images to YCbCr and only utilize the luminance channel as the side information. Following [13], we apply bicubic interpolation as a preprocessing step to upscale the LR input such that the input and output images are of the same size.

2) *NYU v2 RGB-D dataset*: Depth cameras like Microsoft Kinect and time-of-flight (ToF) cameras only provide low-resolution depth images. Therefore, depth upsampling is a necessary task for many vision applications. We apply our models for depth upsampling with the aid of RGB images, using the NYU v2 RGB-D dataset [71]. The dataset contains 1449 RGB images with their depth maps. Similar to [35], we use the first 1000 images for training, and the remaining 449 for testing.

3) *Columbia multi-spectral database*: The third dataset that we use to evaluate the proposed models is the Columbia multi-spectral database,² which contains spectral reflectance data and RGB images. For testing, we reserve 7 images from the 640 nm band and randomly select 7 images from different bands; the rest are used for training.

B. Implementation Details

All networks are designed with three unfolding steps for the target (LMCS-Net) and the side information (ACSC) encoders. The number of unfolding steps is chosen after taking into account the trade-off between the computational complexity and the reconstruction accuracy; for instance, by increasing the unfolding steps to five, the improvement in the average PSNR

¹https://ivrl.epfl.ch/supplementary_material/cvpr11/

²<http://www.cs.columbia.edu/CAVE/databases/multispectral>

TABLE I
SUPER-RESOLUTION OF NIR IMAGES WITH THE AID OF RGB IMAGES. PERFORMANCE COMPARISON [IN TERMS OF AVERAGE PSNR (DB)] OVER ALL TEST IMAGES FOR $\times 2$, $\times 4$ AND $\times 6$ UPSCALING.

Scale	CSCN [44]	ACSC [42]	EDSR [20]	SRFBN [56]	DJF [35]	CoSTA [45]	LMCSC-Net	LMCSC+-Net	LMCSC-ResNet
$\times 2$	36.84	36.92	36.59	36.94	38.78	38.93	39.28	39.42	39.57
$\times 4$	30.64	30.35	31.85	32.11	32.91	33.20	33.96	34.23	34.36
$\times 6$	27.94	27.91	30.49	30.63	29.19	30.88	32.07	31.94	32.33

TABLE II
SUPER-RESOLUTION OF NIR IMAGES WITH THE AID OF RGB IMAGES. PERFORMANCE COMPARISON [IN TERMS OF PSNR (dB) AND SSIM] FOR SELECTED TEST IMAGES FOR $\times 2$, $\times 4$ AND $\times 6$ UPSCALING.

NIR/RGB	u-0004		u-0006		u-0017		o-0018		u-0020		u-0026		o-0030		u-0050		Average		
	PSNR	SSIM																	
$\times 2$																			
Bicubic	30.55	0.9290	36.89	0.9462	34.83	0.9183	30.50	0.9116	32.68	0.9324	30.51	0.9142	30.90	0.8876	30.68	0.9229	32.19	0.9202	
SDF [61]	30.72	0.9290	36.71	0.9364	34.89	0.9139	30.74	0.9128	32.89	0.9317	30.58	0.9110	31.02	0.8816	30.61	0.9125	32.28	0.9161	
CSCN [44]	32.77	0.9715	39.47	0.9715	36.76	0.9574	33.98	0.9659	35.54	0.9658	32.94	0.9339	33.34	0.9465	33.31	0.9693	34.76	0.9602	
ACSC [42]	33.24	0.9723	39.78	0.9718	36.64	0.9579	34.26	0.9670	35.65	0.9660	33.11	0.9416	33.32	0.9465	33.39	0.9696	34.93	0.9608	
EDSR [20]	35.10	0.9971	40.66	0.9958	37.57	0.9942	35.97	0.9961	37.11	0.9968	34.21	0.9941	34.82	0.9939	36.55	0.9956	36.49	0.9954	
SRFBN [56]	35.36	0.9974	41.08	0.9970	38.19	0.9950	36.47	0.9971	37.50	0.9969	31.00	0.9782	35.57	0.9944	37.06	0.9966	36.53	0.9941	
DJF [35]	34.50	0.9964	41.52	0.9975	38.65	0.9961	34.78	0.9960	37.35	0.9973	33.15	0.9939	35.67	0.9944	32.60	0.9928	36.03	0.9955	
CoSTA [45]	35.83	0.9968	42.40	0.9976	39.13	0.9953	37.54	0.9975	39.00	0.9974	34.11	0.9944	36.90	0.9946	33.53	0.9937	37.30	0.9959	
DMSC [48]	36.97	0.9976	43.22	0.9977	40.41	0.9970	37.90	0.9964	40.07	0.9975	34.96	0.9948	37.74	0.9953	33.78	0.9934	38.13	0.9962	
LMCSC-Net	37.26	0.9977	43.60	0.9982	40.87	0.9967	39.21	0.9982	40.98	0.9980	35.60	0.9963	38.29	0.9961	34.11	0.9948	38.74	0.9970	
LMCSC+-Net	37.47	0.9978	43.66	0.9977	40.96	0.9988	39.58	0.9975	40.84	0.9976	35.92	0.9950	38.14	0.9959	34.27	0.9940	38.84	0.9968	
LMCSC-ResNet	37.99	0.9982	43.84	0.9979	40.76	0.9980	40.05	0.9989	41.05	0.9978	36.15	0.9954	38.18	0.9965	34.29	0.9943	39.04	0.9971	
$\times 4$																			
Bicubic	25.93	0.9029	30.89	0.9458	30.45	0.9527	25.19	0.9298	28.03	0.9577	26.27	0.8704	26.54	0.8401	26.65	0.9434	27.49	0.9179	
SDF [61]	26.82	0.9066	30.60	0.8918	30.72	0.9281	26.09	0.9169	29.09	0.9505	26.61	0.8558	27.21	0.8415	27.07	0.9207	28.03	0.9018	
JBF [59]	28.47	0.9359	32.10	0.9311	31.11	0.9172	27.59	0.9308	30.67	0.9523	26.82	0.8627	27.58	0.8476	27.32	0.9099	28.96	0.9109	
JFSM [62]	30.86	0.9721	32.86	0.9741	32.85	0.9500	30.80	0.9774	32.61	0.9797	26.92	0.9332	30.56	0.9064	27.58	0.9251	30.89	0.9522	
GF [60]	28.75	0.9391	32.66	0.9400	31.32	0.9205	27.70	0.9251	30.69	0.9494	26.89	0.8571	27.59	0.8383	27.35	0.9116	29.12	0.9101	
CSCN [44]	27.64	0.9378	32.60	0.9361	31.68	0.9211	27.28	0.9250	30.04	0.9487	27.91	0.8724	27.72	0.8378	28.20	0.9101	29.14	0.9111	
ACSC [42]	27.28	0.9371	32.61	0.9360	31.66	0.9208	27.42	0.9252	29.87	0.9483	27.92	0.8722	27.66	0.8381	27.80	0.9086	29.03	0.9107	
EDSR [20]	28.59	0.9759	33.42	0.9684	32.50	0.9693	28.54	0.9717	31.09	0.9789	28.74	0.9678	28.81	0.9528	29.58	0.9742	30.15	0.9699	
SRFBN [56]	29.01	0.9787	33.73	0.9702	32.91	0.9725	28.88	0.9740	31.44	0.9807	29.10	0.9702	29.45	0.9583	29.89	0.9762	30.55	0.9726	
DJF [35]	31.02	0.9784	36.04	0.9894	34.18	0.9815	30.72	0.9888	33.60	0.9915	29.21	0.9397	31.27	0.9345	28.58	0.9616	31.83	0.9707	
CoSTA [45]	31.56	0.9835	37.21	0.9871	34.87	0.9777	32.35	0.9867	34.75	0.9887	29.94	0.9708	32.28	0.9709	29.42	0.9705	32.80	0.9795	
DMSC [48]	33.19	0.9846	37.69	0.9892	36.00	0.9812	33.84	0.9888	36.33	0.9893	30.65	0.9725	33.19	0.9727	29.85	0.9716	33.84	0.9812	
LMCSC-Net	33.75	0.9869	38.74	0.9912	36.16	0.9828	34.17	0.9902	36.95	0.9900	31.03	0.9784	33.56	0.9780	30.04	0.9772	34.28	0.9843	
LMCSC+-Net	33.89	0.9889	38.69	0.9909	36.13	0.9828	34.54	0.9914	37.08	0.9909	31.21	0.9785	33.66	0.9784	30.07	0.9771	34.39	0.9889	
LMCSC-ResNet	33.80	0.9895	38.77	0.9915	36.54	0.9836	34.78	0.9920	37.34	0.9923	30.95	0.9782	33.59	0.9784	30.10	0.9773	34.49	0.9853	
$\times 6$																			
Bicubic	23.87	0.8094	28.48	0.8671	28.64	0.8998	23.07	0.8393	26.03	0.9053	24.71	0.7850	25.19	0.7515	25.17	0.8921	25.65	0.8437	
SDF [61]	24.62	0.8413	28.76	0.8377	29.13	0.8910	23.79	0.8439	26.93	0.9089	25.17	0.7989	25.80	0.7748	25.90	0.8837	26.26	0.8475	
JBF [59]	25.96	0.8858	30.00	0.8861	29.63	0.8864	25.09	0.8718	28.19	0.9200	25.64	0.8235	26.32	0.7994	26.26	0.8837	27.13	0.8696	
JFSM [62]	27.97	0.9527	32.28	0.9716	32.01	0.9434	27.47	0.9470	30.33	0.9673	27.54	0.9128	29.38	0.8902	26.67	0.9068	29.21	0.9365	
GF [60]	25.94	0.8817	30.17	0.8876	29.61	0.8860	24.98	0.8591	28.01	0.9118	25.63	0.8131	26.22	0.7855	26.26	0.8846	27.10	0.8637	
CSCN [44]	25.01	0.8796	29.94	0.8860	29.53	0.8788	24.57	0.8521	27.46	0.9105	25.79	0.8052	25.86	0.7698	26.71	0.9026	26.86	0.8605	
ACSC [42]	24.82	0.8790	29.97	0.8856	29.48	0.8789	24.70	0.8508	27.49	0.9111	25.97	0.8049	25.91	0.7704	26.43	0.9031	26.85	0.8604	
EDSR [20]	26.52	0.9536	30.60	0.9340	30.55	0.9470	25.67	0.9379	28.56	0.9590	26.96	0.9408	26.76	0.9182	27.58	0.9508	27.90	0.9426	
SRFBN [56]	26.62	0.9559	30.83	0.9342	30.80	0.9500	25.93	0.9385	28.64	0.9591	27.19	0.9422	27.24	0.9225	27.58	0.9502	28.10	0.9441	
DJF [35]	29.68	0.9670	34.92	0.9830	32.80	0.9599	29.92	0.9844	32.61	0.9873	28.38	0.9183	30.00	0.9063	27.64	0.9414	30.75	0.9559	
CoSTA [45]	29.19	0.9686	34.82	0.9769	32.79	0.9549	29.94	0.9755	32.38	0.9791	28.53	0.9487	30.22	0.9479	28.30	0.9539	30.78	0.9632	
DMSC [48]	30.20	0.9734	35.74	0.9815	33.55	0.9778	31.34	0.9796	33.56	0.9822	29.01	0.9603	30.61	0.9584	28.45	0.9591	31.56	0.9715	
LMCSC-Net	31.74	0.9811	36.46	0.9851	34.23	0.9748	32.88	0.9865	35.23	0.9872	29.37	0.9622	31.08	0.9599	28.74	0.9609	32.46	0.9751	
LMCSC+-Net	32.12	0.9840	36.45	0.9850	34.58	0.9759	33.17	0.9873	35.68	0.9888	29.51	0.9628	31.53	0.9631	28.89	0.9622	32.74	0.9762	
LMCSC-ResNet	32.19	0.9846	36.52	0.9860	34.65	0.9763	33.24	0.9877	35.75	0.9889	29.58	0.9630	31.59	0.9638	28.94	0.9624	32.81	0.9766	

is less than 0.1 dB while the execution time is almost 87% higher. In the LMCSC-ResNet, the ACSC branch employed for the nonlinear mapping of the target signal is designed with one unfolding step.

We empirically set the size of the network parameters \mathcal{P} , \mathcal{Q} , \mathcal{G} and \mathcal{T} to $7 \times 7 \times 1 \times 85$; the size of \mathcal{R} and \mathcal{V} are set to $7 \times 7 \times 85 \times 1$. The size of the convolutional dictionaries

for reconstruction is $7 \times 7 \times 85 \times 1$. Note that a convolutional layer of size $k \times k \times c \times g$ consists of g convolutional filters with kernel size k and c channels. We use united weights at every unfolding step, i.e., the t -th layer of LMCSC and ACSC subnetworks is realized by the independent variables \mathcal{R}_t , \mathcal{Q}_t and \mathcal{V}_t , \mathcal{T}_t , respectively. The weights of all layers are initialized randomly using the Gaussian distribution with

standard deviation equal to 0.01. The parameters μ and γ of the proximal operators are both initialized to 0.2. We train the network using the Adam optimizer.

We notice that the complexity of our networks is dominated by the LeSITA activation layers in the LMCSC block, and an implementation based on (8) and (9) is not efficient. In order to address this issue, we rewrite the proximal operator in (8), (9) as follows:

$$\begin{aligned} \xi_\mu(v_i; s_i) = & \text{sign}(s_i)[R(\text{sign}(s_i)v_i - 2\mu - |s_i|) \\ & - R(\text{sign}(s_i)v_i - |s_i|) + R(\text{sign}(s_i)v_i) \\ & - R(-\text{sign}(s_i)v_i - 2\mu)], \end{aligned} \quad (16)$$

where $R(v) = \max(0, v)$ is the Rectified Linear Unit (ReLU) function. This form of the proximal operator results in a 30% faster implementation and we use this version in all of the experiments.

C. Performance Comparison

1) *Super-resolution of NIR/RGB images:* The first set of experiments involves super-resolution of NIR images with the aid of RGB images. The proposed models are compared with several single-modal and multimodal methods. Among the reference single-modal methods, the network designs proposed in [44] and [42] also involve deep unfolding architectures with sparse priors;³ [20] is a residual network, while [56] has an RNN structure. The multimodal designs include [35] and [45]; recall that the latter is a LISTA-based network.

We employ the EPFL RGB-NIR dataset and test our models on 25 NIR/RGB image pairs. Table I presents average results in terms of the Peak Signal-to-Noise Ratio (PSNR) for upscaling factors equal to $\times 2$, $\times 4$ and $\times 6$. We also present detailed PSNR and structural similarity (SSIM) index results for selected test images⁴ in Table II; these images have been used for testing in [33]. As can be seen in Table I, our models deliver higher reconstruction accuracy compared to reference methods at all scales, with LMCSC-ResNet achieving the best performance. Furthermore, the numerical results show that as the upscaling factor increases, the PSNR gain of LMCSC-ResNet over the second best reference method [45] also increases. For instance, at scale $\times 2$ the gain is 0.64dB, and rises to 0.84dB and 1.45dB for scales $\times 4$ and $\times 6$, respectively. The results for selected images in Table II are similar. The average PSNR gain over [45] is 1.7dB at scale $\times 2$, and grows to 1.7dB at scale $\times 4$, and 2.03dB at scale $\times 6$. The role of multimodal fusion becomes more significant as the SR upscaling factor increases; our numerical analysis shows that the proposed models can effectively fuse the information from two different modalities.

2) *Depth upsampling:* For the application of depth map upsampling with the aid of RGB images, we train our LMCSC-ResNet network for three upscaling factors, $\times 4$, $\times 8$ and $\times 16$, using the first 1000 images of the NYU v2 dataset [71]. We

³The model in [42] has been applied to image denoising and inpainting; thus, we slightly modified it and trained it for SR. The number and size of convolutional filters is different than what reported in [42] and we do not force the layers to share weights.

⁴A test image is identified by a letter ‘‘u’’, ‘‘o’’, ‘‘i’’ referring to the folders urban, oldbuilding, indoor in the dataset, and a code ‘‘00xx’’.

report averaged Root Mean Square Error (RMSE) results over 449 test images in Table III and also detailed results for 10 selected images from this dataset in Table IV. Table III involves comparison with several multimodal methods such as the joint filtering approaches JBF [59], GF [60], SDF [61], a learning based method proposed by Gu *et al.* [63], and the deep learning design DJF [35]; the numerical results for the reference methods are provided by the authors of [63]. We select the second and third best methods from Table III, that is, [35] and [63], to compare the performance of our models on selected images in Table IV. We note that for the scales $\times 4$ and $\times 8$, LMCSC₊-Net achieves the lowest average RMSE. However, for an upscaling factor $\times 16$ LMCSC-ResNet has the best performance. At the highest upscaling factor, in the presence of very limited information from the LR input, LMCSC-ResNet has an RMSE gain of 0.36 over the second best method, i.e., Gu *et al.* [63].

3) *Multi-spectral data super-resolution:* We utilize the Columbia multi-spectral dataset for the last set of experiments. We apply LMCSC-ResNet to super-resolve spectral images using their RGB version as side information. The experiments involve comparison of our models against several multimodal methods, namely, JBF [59], GF [60] and SDF [61], which are joint filtering approaches, DJF [35] and CoISTA [45] which are deep learning designs, the method proposed in [62] coined JFSM, and the coupled dictionary learning based method CDLSR [33]. We also report results for the single-modal deep learning designs EDSR [20] and SRFBN [56]. Numerical results are presented in Tables V and VI. Table V includes results for $\times 4$ upsampling in terms of PSNR and SSIM for 7 test images of the 640nm band. We can see that LMCSC-ResNet yields the best performance for scale $\times 4$ with a gain of more than 2.1dB over [45]. Table VI presents detailed results for three different scales, $\times 4$, $\times 8$ and $\times 16$, for randomly selected test images from different bands. Similar to the depth map upsampling application, Table VI shows that for $\times 4$ and $\times 8$ scales LMCSC₊-Net provides the highest average PSNR. For $\times 16$, LMCSC-ResNet delivers the best reconstruction accuracy with a PSNR gain of 2.74dB over [45], the second best method among the competing works.

4) *Visual examples:* We conclude our experiments with visual examples for two super-resolved NIR images, presented in Fig. 7 and Fig. 6, as well as for two super-resolved multi-spectral images, presented in Fig. 8 and Fig. 9. The visual comparison corroborates the presented numerical results.

D. Complexity Analysis

The proposed LMCSC-based networks operate on the entire image rather than reconstructing overlapping patches and aggregating them. The inference time of the proposed networks is independent of the upscaling factor, as the input is first upsampled to the desired resolution using bicubic interpolation. Table VII reports averaged inference running times of the proposed models and CoISTA [45] on 10 test images from the Columbia multi-spectral database with size 512×512 pixels and on 10 images of size 256×256 pixels, which are cropped versions of the previous ones. All models are

TABLE III
 DEPTH UPSAMPLING WITH THE AID OF RGB IMAGES. PERFORMANCE COMPARISON [IN TERMS OF AVERAGE RMSE] OVER 449 TEST IMAGES FROM THE NYU V2 RGB-D DATASET FOR $\times 4$, $\times 8$, AND $\times 16$ UPSAMPLING.

RGB-D	GF [60]	JBF [59]	SDF [61]	DJF [35]	Gu <i>et al.</i> [63]	LMCSC-Net	LMCSC ₊ -Net	LMCSC-ResNet
$\times 4$	4.04	2.31	3.04	1.97	1.56	1.49	1.38	1.45
$\times 8$	7.34	4.12	5.67	3.39	2.99	2.67	2.58	2.61
$\times 16$	12.23	6.98	9.97	5.63	5.24	5.01	4.93	4.88

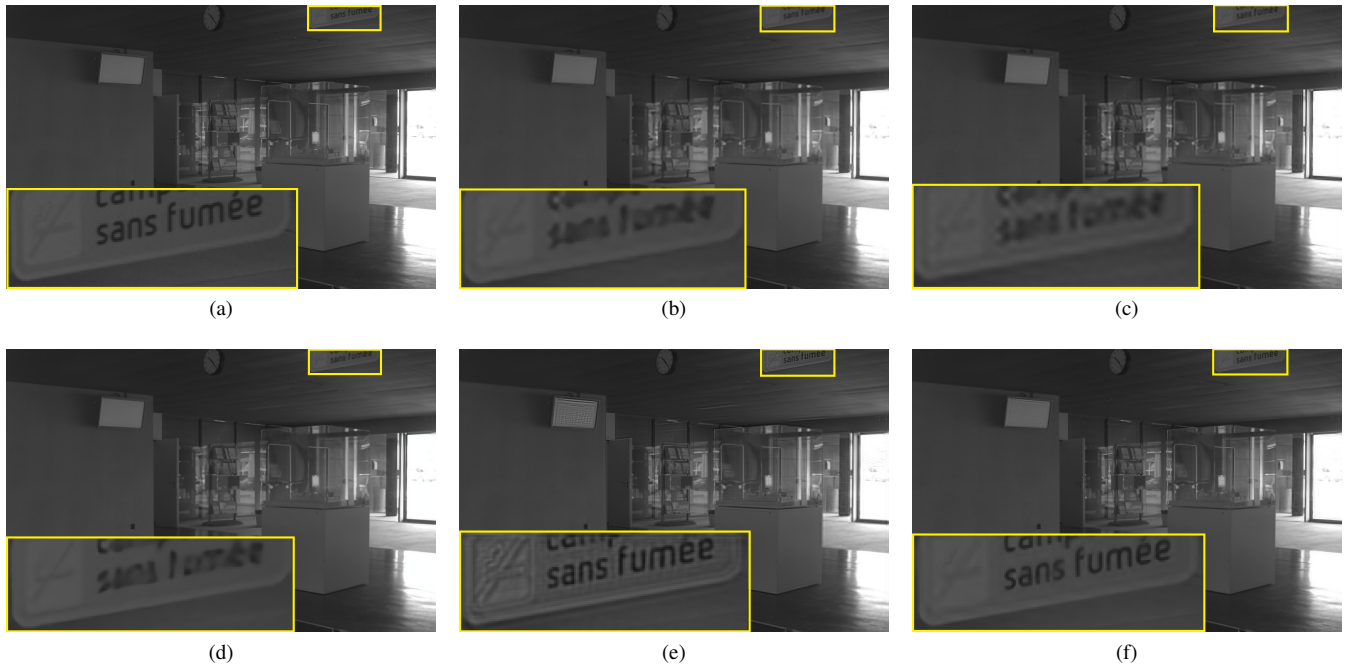


Fig. 6. Super-resolution of the NIR image “i-0013” with upscaling factor $\times 4$. (a) ground-truth (b) CSCN [44], (c) ACSC [42], (d) EDSR [20], (e) DJF [35] and (f) LMCSC-ResNet.

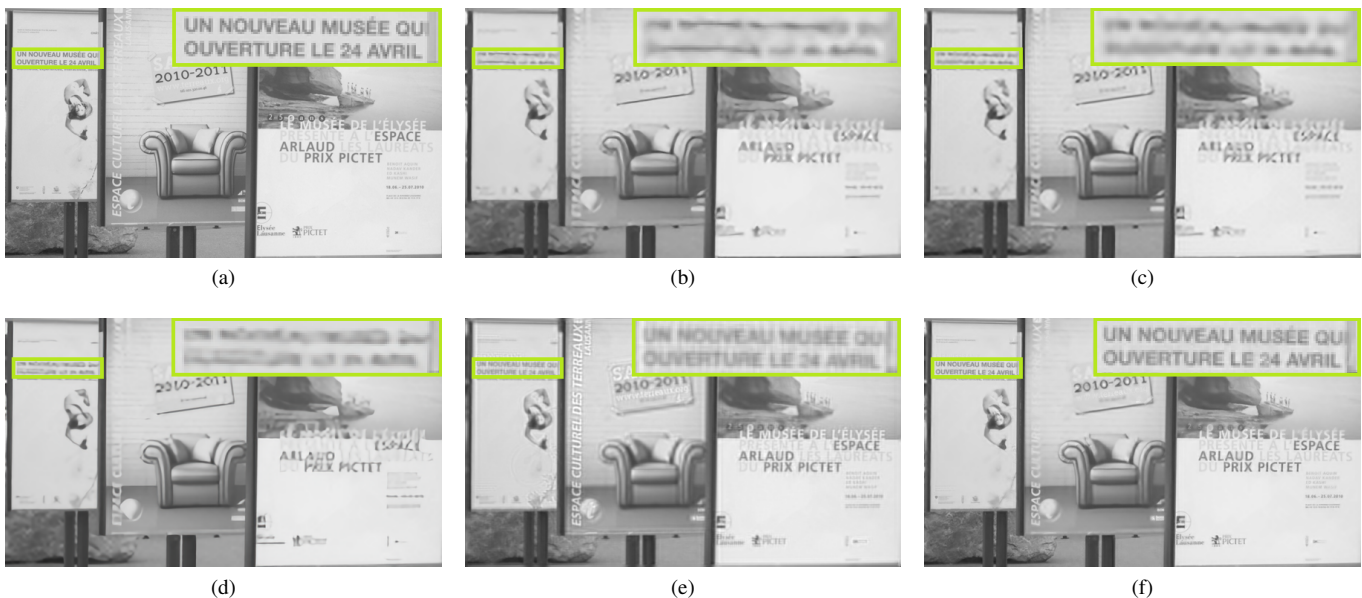


Fig. 7. Super-resolution of the test NIR image “u-0000” with upscaling factor $\times 4$. (a) ground-truth (b) CSCN [44], (c) ACSC [42], (d) EDSR [20], (e) DJF [35] and (f) LMCSC-ResNet. Results for CDLSR [33] are not presented as the code is not available.

TABLE IV
DEPTH UPSAMPLING WITH THE AID OF RGB IMAGES. PERFORMANCE COMPARISON [IN TERMS OF RMSE] OVER SELECTED TEST IMAGES FROM THE NYU V2 DATASET FOR $\times 4$, $\times 8$ AND $\times 16$ UPSAMPLING.

Depth/RGB		NYU-1	NYU-2	NYU-3	NYU-4	NYU-5	NYU-6	NYU-7	NYU-8	NYU-9	NYU-10	Average
$\times 4$	Bicubic	3.70	4.35	2.77	3.73	4.13	4.43	4.31	3.52	3.33	5.20	3.95
	DJF [35]	1.63	2.47	1.31	2.08	2.07	1.77	1.80	1.73	1.55	2.25	1.87
	Gu <i>et al.</i> [63]	1.59	1.53	1.08	1.62	1.78	1.62	2.17	1.57	1.43	2.28	1.66
	LMCSC-Net	1.38	1.08	0.96	1.05	1.57	1.28	1.31	1.29	1.13	1.66	1.28
	LMCSC ₊ -Net	1.35	1.02	0.88	1.04	1.45	1.16	1.28	1.22	1.08	1.39	1.19
	LMCSC-ResNet	1.37	1.13	0.92	1.10	1.50	1.26	1.42	1.24	1.09	1.51	1.26
$\times 8$	Bicubic	6.42	6.16	4.83	6.93	6.94	7.07	7.19	6.11	5.91	8.63	6.62
	DJF [35]	3.04	3.10	2.22	3.96	3.51	2.84	3.00	2.92	2.75	4.41	3.17
	Gu <i>et al.</i> [63]	2.93	3.55	2.12	3.47	2.95	2.87	3.80	2.95	2.50	4.19	3.13
	LMCSC-Net	2.16	2.01	1.47	2.33	2.95	2.18	2.37	2.23	1.81	2.80	2.23
	LMCSC ₊ -Net	2.14	1.96	1.47	2.30	2.86	2.14	2.29	2.23	1.78	2.84	2.20
	LMCSC-ResNet	2.09	1.93	1.42	2.21	2.90	2.15	2.40	2.22	1.75	2.66	2.18
$\times 16$	Bicubic	11.10	11.99	7.88	10.49	11.04	11.59	11.11	10.55	9.86	14.67	11.03
	DJF [35]	5.20	4.23	3.53	6.21	6.10	3.78	5.30	5.00	4.42	6.72	5.05
	Gu <i>et al.</i> [63]	4.95	5.15	3.34	5.61	5.12	4.20	5.45	4.66	4.18	6.80	4.95
	LMCSC-Net	3.86	4.37	3.55	4.59	5.53	4.18	4.53	3.86	3.61	6.03	4.41
	LMCSC ₊ -Net	3.80	4.12	3.32	4.61	5.48	4.01	4.23	3.84	3.55	5.82	4.29
	LMCSC-ResNet	3.94	3.89	3.16	4.85	4.73	3.54	4.18	3.87	3.37	5.87	4.15

TABLE V
SUPER-RESOLUTION OF MULTI-SPECTRAL IMAGES WITH THE AID OF RGB IMAGES. PERFORMANCE COMPARISON [IN TERMS OF PSNR (DB) AND SSIM] FOR SELECTED MULTI-SPECTRAL TEST IMAGES FROM 640NM BAND FOR $\times 4$ UPSAMPLING.

$\times 4$	Chart toy		Egyptian		Feathers		Glass tiles		Jelly beans		Oil Paintings		Paints		Average	
	PSNR	SSIM	PSNR	SSIM	PSNR	SSIM	PSNR	SSIM								
Bicubic	29.14	0.9451	36.22	0.9761	30.46	0.9530	26.38	0.92156	27.45	0.9269	32.23	0.9025	30.47	0.9569	30.39	0.9403
SDF [61]	30.74	0.9523	37.16	0.9677	30.92	0.9434	27.01	0.9188	27.87	0.9279	32.80	0.9001	31.35	0.9569	31.12	0.9381
JBF [59]	30.69	0.9528	37.82	0.9788	31.80	0.9599	27.15	0.9339	28.97	0.9474	33.23	0.9034	32.08	0.9714	31.68	0.9497
JFSM [62]	33.30	0.9215	39.68	0.9428	33.54	0.9096	29.34	0.9407	30.82	0.9356	34.16	0.9439	32.96	0.9321	33.40	0.9323
GF [60]	30.70	0.9514	37.96	0.9788	32.12	0.9618	27.45	0.9326	29.54	0.9488	33.30	0.9033	32.23	0.9698	31.90	0.9494
EDSR [20]	33.57	0.9926	39.42	0.9941	35.11	0.9927	29.41	0.9822	32.67	0.9917	33.40	0.9676	37.33	0.9955	34.42	0.9880
SRFBN [56]	33.61	0.9925	39.44	0.9942	35.10	0.9933	29.35	0.9823	32.74	0.9919	33.42	0.9677	37.23	0.9957	34.41	0.9882
DJF [35]	33.91	0.9842	41.31	0.9861	36.01	0.9848	31.83	0.9814	32.77	0.9820	34.39	0.9493	37.74	0.9897	35.43	0.9796
CoISTA [45]	36.63	0.9937	41.19	0.9948	36.42	0.9913	30.63	0.9848	34.37	0.9919	35.43	0.9791	34.84	0.9928	35.64	0.9898
LMCSC-Net	38.47	0.9962	42.47	0.9956	38.32	0.9953	33.52	0.9936	36.75	0.9955	36.78	0.9844	36.44	0.9955	37.53	0.9937
LMCSC ₊ -Net	38.01	0.9959	43.10	0.9958	37.94	0.9950	33.73	0.9936	36.89	0.9956	36.32	0.9838	36.28	0.9956	37.47	0.9936
LMCSC-ResNet	38.30	0.9958	43.45	0.9958	38.14	0.9949	33.72	0.9932	36.83	0.9956	36.94	0.9846	36.95	0.9961	37.76	0.9937

tested on an NVIDIA GeForce GTX 1070. We observe that our proposed networks have higher inference times compared to CoISTA [45], which is due to the proposed fusion strategy. Specifically, CoISTA [45] fuses modalities in the last layer of the network by a linear combination of the sparse representations. In contrast, the LMCSC layers of our networks perform intermediate fusion using the activation function defined in (8) and (9). As demonstrated by the reconstruction accuracy results, where gains of up to 2.74dB over CoISTA [45] were reported, the proposed fusion approach can effectively capture the complex relationships across modalities at the expense of a reasonable increase in terms of computation.

VII. CONCLUSIONS

In this paper, we presented a new approach for guided image super-resolution based on a novel multimodal deep unfolding design. The efficient integration of the guidance modality into the deep learning architecture is achieved with a neural network that performs steps similar to an iterative algorithm for convolutional sparse coding with side information. By exploiting residual learning, we further improve

the training efficiency and increase reconstruction accuracy of the proposed framework. Our approach was applied to super-resolution of NIR images, multi-spectral and depth maps with the aid of HR RGB images. The superior performance of our models against various state-of-the-art single-modal and multimodal methods was demonstrated by experimental results.

REFERENCES

- [1] A. Ribes and F. Schmitt, "Linear inverse problems in imaging," *IEEE Signal Processing Magazine*, vol. 25, no. 4, pp. 84–99, 2008.
- [2] A. Lucas, M. Iliadis, R. Molina, and A. K. Katsaggelos, "Using deep neural networks for inverse problems in imaging: Beyond analytical methods," *IEEE Signal Processing Magazine*, vol. 35, no. 1, pp. 20–36, 2018.
- [3] J. Yang, J. Wright, T. S. Huang, and Y. Ma, "Image super-resolution via sparse representation," *IEEE Transactions on Image Processing*, vol. 19, pp. 2861–2873, 2010.
- [4] J. Yang, Z. Wang, Z. Lin, S. Cohen, and T. S. Huang, "Coupled dictionary training for image super-resolution," *IEEE Transactions on Image Processing*, vol. 21, no. 8, pp. 3467–3478, 2012.
- [5] R. Timofte, V. D. Smet, and L. V. Gool, "Anchored neighborhood regression for fast example-based super-resolution," in *IEEE International Conference on Computer Vision (ICCV)*, 2013.

TABLE VI
SUPER-RESOLUTION OF MULTI-SPECTRAL IMAGES WITH THE AID OF RGB IMAGES. PERFORMANCE COMPARISON [IN TERMS OF PSNR (DB) AND SSIM] OVER SELECTED MULTI-SPECTRAL TEST IMAGES (FROM DIFFERENT BANDS) FOR $\times 4$, $\times 8$ AND $\times 16$ UPSCALING.

MS/RGB	Chart toy		Egyptian		Feathers		Glass tiles		Jelly beans		Oil Paintings		Paints		Average	
	PSNR	SSIM	PSNR	SSIM	PSNR	SSIM	PSNR	SSIM								
$\times 4$																
Bicubic	28.94	0.9424	36.57	0.9786	30.80	0.9562	26.65	0.9242	27.81	0.9302	31.67	0.8943	29.29	0.9493	30.25	0.9393
SDF [61]	31.87	0.9694	39.43	0.9795	33.45	0.9650	28.22	0.9374	30.32	0.9433	32.86	0.9126	31.96	0.9655	32.59	0.9532
JBF [59]	32.56	0.9653	38.73	0.9735	33.60	0.9637	27.52	0.9341	30.29	0.9498	32.77	0.8962	31.94	0.9699	32.49	0.9504
JFSM [62]	32.98	0.9295	40.39	0.9705	33.89	0.9425	28.98	0.9397	31.18	0.9451	35.91	0.9560	32.76	0.9430	33.73	0.9466
GF [60]	34.09	0.9788	40.24	0.9796	33.60	0.9748	29.46	0.9593	30.90	0.9658	35.03	0.9441	31.73	0.9702	33.58	0.9675
EDSR [20]	33.45	0.9836	40.03	0.9829	35.55	0.9875	29.75	0.9736	32.81	0.9838	32.69	0.9178	37.28	0.9914	34.51	0.9739
SRFBN [56]	33.43	0.9838	40.04	0.9822	35.53	0.9873	29.53	0.9676	32.97	0.9845	32.68	0.9182	36.06	0.9907	34.32	0.9735
DGF [36]	34.19	0.9559	37.81	0.9620	31.22	0.9336	29.93	0.9339	28.94	0.9459	36.10	0.9649	31.72	0.9680	32.84	0.9520
DJF [35]	37.86	0.9935	45.69	0.9922	40.13	0.9939	34.97	0.9915	39.16	0.9885	37.76	0.9805	39.36	0.9944	39.28	0.9906
CoISTA [45]	36.58	0.9914	45.91	0.9961	39.62	0.9937	33.99	0.9907	38.92	0.9956	37.26	0.9690	38.40	0.9949	38.67	0.9902
LMCSC-Net	40.31	0.9965	48.79	0.9981	41.48	0.9962	34.65	0.9939	39.75	0.9966	39.14	0.9910	38.98	0.9966	40.44	0.9955
LMCSC ₊ -Net	40.81	0.9977	49.28	0.9989	41.53	0.9969	34.83	0.9946	40.10	0.9975	38.94	0.9915	38.92	0.9975	40.63	0.9964
LMCSC-ResNet	40.47	0.9974	47.99	0.9989	41.60	0.9969	34.96	0.9943	39.80	0.9973	39.39	0.9863	39.53	0.9978	40.53	0.9956
$\times 8$																
Bicubic	25.00	0.8048	33.12	0.9316	25.59	0.8067	22.56	0.7308	23.04	0.7388	30.56	0.8234	26.40	0.8465	26.61	0.8118
SDF [61]	27.89	0.8933	34.22	0.9366	28.25	0.8967	24.66	0.8253	24.88	0.8527	31.61	0.8587	28.54	0.9246	28.58	0.8840
JBF [59]	28.00	0.9092	35.92	0.9578	26.48	0.8492	23.06	0.7706	24.74	0.8532	31.90	0.8531	28.21	0.9135	28.33	0.8723
JFSM [62]	30.28	0.8897	38.31	0.9451	28.24	0.9043	25.31	0.8851	26.59	0.9083	32.55	0.9199	29.97	0.9339	30.18	0.9123
GF [60]	29.77	0.9446	36.52	0.9627	27.85	0.9183	25.24	0.8641	25.05	0.8813	33.82	0.9383	29.25	0.9451	29.64	0.9221
EDSR [20]	27.04	0.8802	35.62	0.9511	28.38	0.9040	23.53	0.8339	24.73	0.8259	31.95	0.8632	30.33	0.9425	28.78	0.8858
SRFBN [56]	27.90	0.8736	35.50	0.9755	30.14	0.9718	23.72	0.9002	25.80	0.9243	31.07	0.9258	28.03	0.9653	28.88	0.9338
DGF [36]	28.39	0.8901	34.98	0.9444	26.83	0.8353	25.46	0.8987	25.97	0.8852	33.25	0.9351	27.89	0.9128	28.97	0.9002
DJF [35]	32.89	0.9733	41.58	0.9850	31.50	0.9396	29.53	0.9685	30.14	0.9503	35.12	0.9492	31.86	0.9553	33.23	0.9602
CoISTA [45]	33.18	0.9768	43.46	0.9906	32.04	0.9493	27.96	0.9390	30.69	0.9585	35.99	0.9482	33.05	0.9679	33.77	0.9615
LMCSC-Net	34.35	0.9805	43.90	0.9966	36.81	0.9875	30.20	0.9724	34.70	0.9888	36.27	0.9759	35.06	0.9910	35.90	0.9847
LMCSC ₊ -Net	34.71	0.9820	44.18	0.9967	37.36	0.9878	30.21	0.9717	34.89	0.9896	36.46	0.9758	36.07	0.9930	36.27	0.9852
LMCSC-ResNet	35.24	0.9835	43.84	0.9966	37.01	0.9888	30.30	0.9756	35.07	0.9898	36.22	0.9737	35.41	0.9917	36.16	0.9857
$\times 16$																
Bicubic	22.36	0.6753	30.32	0.8555	23.96	0.7402	21.75	0.6121	18.70	0.4277	27.66	0.6889	20.95	0.5975	23.67	0.6567
SDF [61]	24.98	0.8366	33.05	0.9298	26.87	0.8623	23.69	0.7854	20.89	0.7212	29.69	0.8778	23.96	0.8547	26.16	0.8383
JBF [59]	24.07	0.8100	32.43	0.9113	25.66	0.8289	22.34	0.6996	19.97	0.6264	28.87	0.7747	23.14	0.7894	25.21	0.7772
JFSM [62]	27.54	0.8617	36.01	0.9294	27.79	0.8750	25.04	0.8682	24.05	0.8773	31.76	0.9104	27.38	0.8400	28.51	0.8803
GF [60]	25.80	0.8834	33.71	0.9347	27.58	0.8840	24.54	0.8130	21.41	0.7912	31.87	0.9096	25.54	0.8822	27.21	0.8712
SRFBN [56]	23.78	0.8203	32.32	0.9452	25.11	0.8816	22.49	0.7643	20.70	0.7144	28.78	0.8483	24.78	0.9085	25.42	0.8404
DGF [36]	26.83	0.8330	33.64	0.9378	25.25	0.8127	24.16	0.8690	23.23	0.8543	31.84	0.9332	26.16	0.8654	27.30	0.8722
DJF [35]	30.03	0.9582	38.82	0.9692	31.03	0.9370	29.08	0.9660	25.43	0.8992	33.04	0.9171	30.58	0.9401	28.59	0.9174
CoISTA [45]	29.85	0.9500	39.18	0.9760	31.07	0.9433	27.82	0.9231	26.66	0.9013	33.95	0.9239	31.06	0.9484	29.50	0.9258
LMCSC-Net	31.52	0.9716	41.43	0.9916	32.29	0.9655	27.29	0.9328	28.42	0.9632	32.96	0.9421	31.14	0.9757	32.14	0.9632
LMCSC ₊ -Net	31.31	0.9688	41.06	0.9928	32.45	0.9694	27.16	0.9310	28.72	0.9640	32.23	0.9364	31.25	0.9784	32.03	0.9630
LMCSC-ResNet	31.69	0.9721	41.51	0.9923	32.67	0.9692	27.48	0.9336	28.75	0.9624	33.16	0.9413	30.44	0.9746	32.24	0.9636

TABLE VII

COMPARISON OF THE INFERENCE TIME (SEC) OF OUR MULTIMODAL ARCHITECTURES AND CoISTA [45] W.R.T. TWO INPUT RESOLUTIONS.

input size	CoISTA [45]	LMCSC-Net	LMCSC ₊ -Net	LMCSC-ResNet
256 \times 256	0.51	1.09	1.14	1.14
512 \times 512	0.63	1.29	1.38	1.39

- [6] —, “A+: Adjusted anchored neighborhood regression for fast super-resolution,” in *Asian Conference on Computer Vision (ACCV)*, 2014.
- [7] J. Yang, J. Wright, T. Huang, and Y. Ma, “Image super-resolution as sparse representation of raw image patches,” in *IEEE Conference on Computer Vision and Pattern Recognition (CVPR)*, 2008.
- [8] K. Jia, X. Wang, and X. Tang, “Image transformation based on learning dictionaries across image spaces,” *IEEE Transactions on Pattern Analysis and Machine Intelligence*, vol. 35, no. 2, pp. 367–380, 2012.
- [9] S. Gu, W. Zuo, Q. Xie, D. Meng, X. Feng, and L. Zhang, “Convolutional sparse coding for image super-resolution,” in *IEEE International Conference on Computer Vision (ICCV)*, 2015.
- [10] K. I. Kim and Y. Kwon, “Single-image super-resolution using sparse regression and natural image prior,” *IEEE Transactions on Pattern*

Analysis and Machine Intelligence, vol. 32, no. 6, pp. 1127–1133, 2010.

- [11] J. Sun, Z. Xu, and H. Y. Shum, “Image super-resolution using gradient profile prior,” in *IEEE Conference on Computer Vision and Pattern Recognition (CVPR)*, 2008.
- [12] D. M. Nguyen, E. Tsiligiani, and N. Deligiannis, “Deep learning sparse ternary projections for compressed sensing of images,” in *IEEE Global Conference on Signal and Information Processing (GlobalSIP)*, 2017.
- [13] C. Dong, C. C. Loy, K. He, and X. Tang, “Image super-resolution using deep convolutional networks,” *IEEE Transactions on Pattern Analysis and Machine Intelligence*, vol. 38, no. 2, pp. 295–307, 2016.
- [14] C. Dong, C. C. Loy, and X. Tang, “Accelerating the super-resolution convolutional neural network,” in *European Conference on Computer Vision (ECCV)*, 2016.
- [15] J. Kim, J. K. Lee, and K. M. Lee, “Accurate image super-resolution using very deep convolutional networks,” in *IEEE Conference on Computer Vision and Pattern Recognition (CVPR)*, 2016.
- [16] J. Kim, J. Kwon Lee, and K. Mu Lee, “Deeply-recursive convolutional network for image super-resolution,” in *IEEE Conference on Computer Vision and Pattern Recognition (CVPR)*, 2016.
- [17] X. Mao, C. Shen, and Y.-B. Yang, “Image restoration using very deep convolutional encoder-decoder networks with symmetric skip connections,” in *Advances in neural information Processing systems (NIPS)*, 2016.
- [18] J. Bruna, P. Sprechmann, and Y. LeCun, “Super-resolution with deep

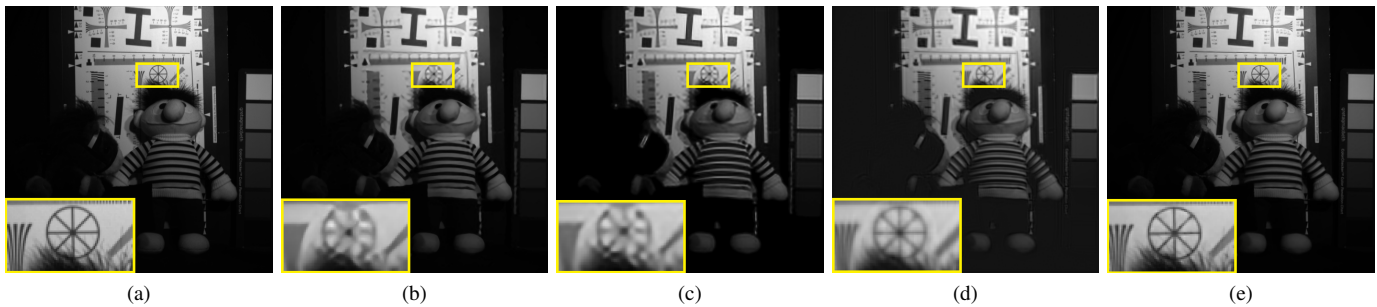


Fig. 8. Super-resolution of the test multi-spectral image “chart” with upscaling factor $\times 4$. (a) ground-truth, (b) CSCN [44], (c) ACSC [42], (d) DJF [35] and (e) LMCS-ResNet.

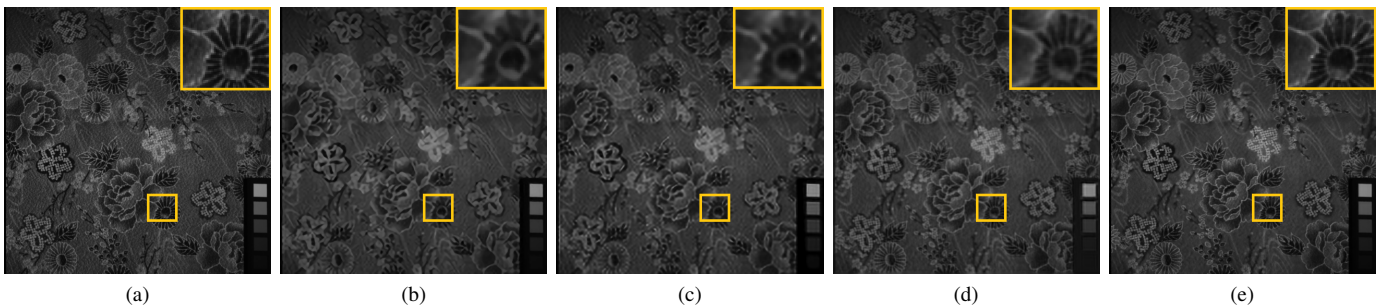


Fig. 9. Super-resolution of the test multi-spectral image “cloth” with upscaling factor $\times 4$. (a) ground-truth, (b) CSCN [44], (c) ACSC [42], (d) DJF [35] and (e) LMCS-ResNet.

convolutional sufficient statistics,” *CoRR*, vol. abs/1511.05666, 2015.

- [19] K. He, X. Zhang, S. Ren, and J. Sun, “Deep residual learning for image recognition,” in *IEEE Conference on Computer Vision and Pattern Recognition (CVPR)*, 2016.
- [20] B. Lim, S. Son, H. Kim, S. Nah, and K. Mu Lee, “Enhanced deep residual networks for single image super-resolution,” in *IEEE Conference on Computer Vision and Pattern Recognition (CVPR) Workshops*, 2017.
- [21] Y. Zhang, K. Li, K. Li, L. Wang, B. Zhong, and Y. Fu, “Image super-resolution using very deep residual channel attention networks,” in *European Conference on Computer Vision (ECCV)*, 2018.
- [22] Y. Tai, J. Yang, and X. Liu, “Image super-resolution via deep recursive residual network,” in *IEEE Conference on Computer Vision and Pattern Recognition (CVPR)*, 2017.
- [23] Y. Tai, J. Yang, X. Liu, and C. Xu, “MemNet: A persistent memory network for image restoration,” in *IEEE International Conference on Computer Vision (ICCV)*, 2017.
- [24] Y. Zhang, Y. Tian, Y. Kong, B. Zhong, and Y. Fu, “Residual dense network for image super-resolution,” in *IEEE Conference on Computer Vision and Pattern Recognition (CVPR)*, 2018.
- [25] S. Wang, L. Zhang, Y. Liang, and Q. Pan, “Semi-coupled dictionary learning with applications to image super-resolution and photo-sketch synthesis,” in *IEEE Conference on Computer Vision and Pattern Recognition (CVPR)*, 2012.
- [26] Y. T. Zhuang, Y. F. Wang, F. Wu, Y. Zhang, and W. M. Lu, “Supervised coupled dictionary learning with group structures for multi-modal retrieval,” in *Twenty-Seventh AAAI Conference on Artificial Intelligence*, 2013.
- [27] X. Liu, M. Song, D. Tao, X. Zhou, C. Chen, and J. Bu, “Semi-supervised coupled dictionary learning for person re-identification,” in *IEEE Conference on Computer Vision and Pattern Recognition (CVPR)*, 2014.
- [28] X.-Y. Jing, X. Zhu, F. Wu, X. You, Q. Liu, D. Yue, R. Hu, and B. Xu, “Super-resolution person re-identification with semi-coupled low-rank discriminant dictionary learning,” in *IEEE Conference on Computer Vision and Pattern Recognition (CVPR)*, 2015.
- [29] M. Dao, N. H. Nguyen, N. M. Nasrabadi, and T. D. Tran, “Collaborative multi-sensor classification via sparsity-based representation,” *IEEE Transactions on Signal Processing*, vol. 64, no. 9, pp. 2400–2415, 2016.
- [30] S. Bahrapour, N. M. Nasrabadi, A. Ray, and W. K. Jenkins, “Multimodal task-driven dictionary learning for image classification,” *IEEE Transactions on Image Processing*, vol. 25, no. 1, pp. 24–38, 2015.
- [31] N. Deligiannis, J. F. Mota, B. Cornelis, M. R. Rodrigues, and I. Daubechies, “Multi-modal dictionary learning for image separation with application in art investigation,” *IEEE Transactions on Image Processing*, vol. 26, no. 2, pp. 751–764, 2016.
- [32] —, “X-ray image separation via coupled dictionary learning,” in *IEEE International Conference on Image Processing (ICIP)*, 2016.
- [33] P. Song, X. Deng, J. F. Mota, N. Deligiannis, P.-L. Dragotti, and M. Rodrigues, “Multimodal image super-resolution via joint sparse representations induced by coupled dictionaries,” *IEEE Transactions on Computational Imaging*, 2019.
- [34] J. Ngiam, A. Khosla, M. Kim, J. Nam, H. Lee, and A. Y. Ng, “Multimodal deep learning,” in *IEEE International Conference on Machine Learning (ICML)*, 2011.
- [35] Y. Li, J. B. Huang, N. Ahuja, and M. H. Yang, “Deep joint image filtering,” in *European Conference on Computer Vision (ECCV)*, 2016.
- [36] H. Wu, S. Zheng, J. Zhang, and K. Huang, “Fast end-to-end trainable guided filter,” in *IEEE Conference on Computer Vision and Pattern Recognition (CVPR)*, 2018.
- [37] K. Gregor and Y. LeCun, “Learning fast approximations of sparse coding,” in *IEEE International Conference on Machine Learning (ICML)*, 2010.
- [38] J. R. Hershey, J. L. Roux, and F. Wenginger, “Deep unfolding: Model-based inspiration of novel deep architectures,” *arXiv preprint arXiv:1409.2574*, 2014.
- [39] B. Xin, Y. Wang, W. Gao, D. Wipf, and B. Wang, “Maximal sparsity with deep networks?” in *Advances in Neural Information Processing Systems (NIPS)*, 2016.
- [40] M. Borgerding, P. Schniter, and S. Rangan, “AMP-inspired deep networks for sparse linear inverse problems,” *IEEE Transactions on Signal Processing*, vol. 65, no. 16, pp. 4293–4308, 2017.
- [41] Y. Yang, J. Sun, H. Li, and Z. Xu, “Deep ADMM-Net for compressive sensing MRI,” in *Advances in Neural Information Processing Systems (NIPS)*, 2016.
- [42] H. Sreter and R. Giryès, “Learned convolutional sparse coding,” in *IEEE International Conference on Acoustics, Speech, and Signal Processing (ICASSP)*, 2018.
- [43] J. Zhang and B. Ghanem, “ISTA-Net: Interpretable optimization-inspired

- deep network for image compressive sensing,” in *IEEE Conference on Computer Vision and Pattern Recognition (CVPR)*, 2018.
- [44] D. Liu, Z. Wang, B. Wen, J. Yang, W. Han, and T. S. Huang, “Robust single image super-resolution via deep networks with sparse prior,” *IEEE Transactions on Image Processing*, vol. 25, no. 7, pp. 3194–3207, 2016.
- [45] X. Deng and P. L. Dragotti, “Deep coupled ISTA network for multi-modal image super-resolution,” *IEEE Transactions on Image Processing*, vol. 29, pp. 1683–1698, 2020.
- [46] —, “Deep convolutional neural network for multi-modal image restoration and fusion,” *arXiv preprint arXiv:1910.04066*, 2019.
- [47] E. Tsiliogianni and N. Deligiannis, “Deep coupled-representation learning for sparse linear inverse problems with side information,” *IEEE Signal Processing Letters*, 2019.
- [48] I. Marivani, E. Tsiliogianni, B. Cornelis, and N. Deligiannis, “Multimodal image super-resolution via deep unfolding with side information,” in *European Signal Processing Conference (EUSIPCO)*, 2019.
- [49] —, “Learned multimodal convolutional sparse coding for guided image super-resolution,” in *IEEE International Conference on Image Processing (ICIP)*, 2019.
- [50] A. Sanchez-Beato and G. Pajares, “Noniterative interpolation-based super-resolution minimizing aliasing in the reconstructed image,” *IEEE Transactions on Image Processing*, vol. 17, no. 10, pp. 1817–1826, 2008.
- [51] F. Zhou, W. Yang, and Q. Liao, “Interpolation-based image super-resolution using multisurface fitting,” *IEEE Transactions on Image Processing*, vol. 21, no. 7, pp. 3312–3318, 2012.
- [52] F. Ling, Y. Du, X. Li, W. Li, F. Xiao, and Y. Zhang, “Interpolation-based super-resolution land cover mapping,” *Remote Sensing Letters*, vol. 4, no. 7, pp. 629–638, 2013.
- [53] J. Yang, Z. Lin, and S. Cohen, “Fast image super-resolution based on in-place example regression,” in *IEEE Conference on Computer Vision and Pattern Recognition (CVPR)*, 2013.
- [54] W. Dong, L. Zhang, G. Shi, and X. Li, “Nonlocally centralized sparse representation for image restoration,” *IEEE Transactions on Image Processing*, vol. 22, no. 4, pp. 1620–1630, 2012.
- [55] S. Mallat and G. Yu, “Super-resolution with sparse mixing estimators,” *IEEE Transactions on Image Processing*, vol. 19, no. 11, pp. 2889–2900, 2010.
- [56] Y. Li, J. Yang, Z. Liu, X. Yang, G. Jeon, and W. Wu, “Feedback network for image super-resolution,” in *IEEE Conference on Computer Vision and Pattern Recognition (CVPR)*, 2019.
- [57] W. Han, S. Chang, D. Liu, M. Yu, M. Witbrock, and T. S. Huang, “Image super-resolution via dual-state recurrent networks,” in *IEEE Conference on Computer Vision and Pattern Recognition (CVPR)*, 2018.
- [58] I. Daubechies, M. Defrise, and C. D. Mol, “An iterative thresholding algorithm for linear inverse problems with a sparsity constrain,” *Communications on Pure and Applied Mathematics*, vol. 57, 11 2004.
- [59] J. Kopf, M. F. Cohen, D. Lischinski, and M. Uyttendaele, “Joint bilateral upsampling,” *ACM Transactions on Graphics (Proceedings of SIGGRAPH)*, 2007.
- [60] K. He, J. Sun, and X. Tang, “Guided image filtering,” *IEEE Transactions on Pattern Analysis and Machine Intelligence*, vol. 35, no. 6, pp. 1397–1409, 2013.
- [61] B. Ham, M. Cho, and J. Ponce, “Robust guided image filtering using nonconvex potentials,” *IEEE Transactions on Pattern Analysis and Machine Intelligence*, vol. 40, no. 1, pp. 192–207, 2018.
- [62] X. Shen, Q. Yan, L. Xu, L. Ma, and J. Jia, “Multispectral joint image restoration via optimizing a scale map,” *IEEE Transactions on Pattern Analysis and Machine Intelligence*, vol. 37, no. 12, pp. 2518–2530, 2015.
- [63] S. Gu, W. Zuo, S. Guo, Y. Chen, C. Chen, and L. Zhang, “Learning dynamic guidance for depth image enhancement,” in *IEEE Conference on Computer Vision and Pattern Recognition (CVPR)*, 2017.
- [64] J. Tropp and S. Wright, “Computational methods for sparse solution of linear inverse problems,” *Proceedings of the IEEE*, 2010.
- [65] M. D. Zeiler, D. Krishnan, G. W. Taylor, and R. Fergus, “Deconvolutional networks,” in *IEEE Conference on Computer Vision and Pattern Recognition (CVPR)*, 2010.
- [66] B. Wohlberg, “Efficient convolutional sparse coding,” in *IEEE International Conference on Acoustics, Speech and Signal Processing (ICASSP)*, 2014.
- [67] F. Heide, W. Heidrich, and G. Wetzstein, “Fast and flexible convolutional sparse coding,” in *IEEE Conference on Computer Vision and Pattern Recognition (CVPR)*, 2015.
- [68] J. F. C. Mota, N. Deligiannis, and M. R. D. Rodrigues, “Compressed sensing with prior information: Strategies, geometry, and bounds,” *IEEE Transaction on Information Theory*, vol. 63, pp. 4472–4496, 2017.
- [69] L. Weizman, Y. C. Eldar, and D. B. Bashat, “Compressed sensing for longitudinal MRI: An adaptive-weighted approach,” *Medical Physics*, vol. 42, no. 9, pp. 5195–5208, 2015.
- [70] J. F. C. Mota, N. Deligiannis, A. C. Sankaranarayanan, V. Cevher, and M. R. D. Rodrigues, “Dynamic sparse state estimation using $\ell_1 - \ell_1$ minimization: Adaptive-rate measurement bounds, algorithms and applications,” in *IEEE International Conference on Acoustics, Speech, and Signal Processing (ICASSP)*, 2015.
- [71] P. K. N. Silberman, D. Hoiem and R. Fergus, “Indoor segmentation and support inference from RGBD images,” in *European Conference on Computer Vision (ECCV)*, 2012.